Astron. Astrophys. 338, 1015–1030 (1998)

ASTRONOMY AND ASTROPHYSICS

The β Pictoris circumstellar disk

XXV. The Ca II absorption lines and the Falling Evaporating Bodies model revisited using UHRF observations⋆

H. Beust[1], **A.-M. Lagrange**[1,2], **I.A. Crawford**[3], **C. Goudard, J. Spyromilio**[4], **and A. Vidal-Madjar**[2]

[1] Laboratoire d'Astrophysique de l'Observatoire de Grenoble, Université J. Fourier, B.P. 53, F-38041 Grenoble Cedex 9, France
[2] Institut d'Astrophysique de Paris, CNRS, 98 bis boulevard Arago, F-75014 Paris, France
[3] Department of Physics and Astronomy, University College London, Gower Street, London WC1E 6BT, UK
[4] E.S.O., Karl-Schwarzschild-Strasse 2, D-8046 Garching bei München, Germany

Received 26 February 1998 / Accepted 3 July 1998

Abstract. We present here ultra high resolution observations of the Ca II K and H lines towards β Pictoris recorded over a period of 3 years and a smaller set of calcium triplet data.

At the present resolution, the central Ca II circumstellar absorption is complex, with several variable components, some of them at very low velocity shifts ($< 10\,\mathrm{km\,s^{-1}}$) with respect to the star, in addition to a very narrow stable component. The stable component is analyzed and physical informations are derived. The variable components at low redshifts are analyzed, and well modeled in the framework of the Falling Evaporating Bodies (FEB) scenario previously invoked to explain the absorption features observed at higher redshifts.

We show that the very low redshift events are well simulated by FEBs crossing the line of sight at somewhat larger distances from the star than those responsible for the higher velocity redshift events. The implications of these new observations on the dynamical process responsible for the FEB phenomenon are discussed. In particular, they put strong constraints on the orbital parameters of the incoming bodies that appear in fact in perfect agreement with an origin based on mean-motion resonances with a massive planet.

Key words: comets: general – stars: circumstellar matter – stars: individual: Beta Pic

1. Introduction

The dusty and gaseous disk discovered around the southern star β Pictoris (Smith & Terrile, 1984) is regarded today as an obvious candidate for a young planetary system. Thanks to a favourable edge-on orientation, the gaseous counterpart of this disk was observed in absorption spectroscopy, revealing strong circumstellar lines (Vidal-Madjar et al., 1986). The survey of these lines (Ca II, Mg II, Fe II, etc...) revealed that apart from a deep central stable component, transient absorption features, usually redshifted, were able to frequently appear or disappear. These additional features are subject to evolve within one day or even less (Vidal-Madjar et al., 1994; Lagrange et al., 1996).

These repeated spectral events have been interpreted as the signature of the evaporation of kilometer-sized bodies in the vicinity of the star. Since the presumed bodies are moving towards the star on star-grazing orbits, this model has been termed the Falling Evaporating Body (FEB) scenario. This scenario has been extensively studied in the past years. Dynamical simulations reproduce the observed events in many of their characteristic details (Beust et al., 1990, 1996).

While the transient events seemed to be well explained by the FEB scenario, the origin of the central stable component was still unclear. Recently, Lagrange et al. (1998) presented a detailed study of the origin of this component. The first outcome of this study was that the refractory elements in this gas have solar relative abundances, while the volatile species appear somewhat depleted. From a dynamical point of view, this study showed that the gas responsible for this absorption, probably located at a moderate distance from the star (0.5–1 A.U.), must be continuously replenished by an internal source, and the FEBs are in fact possible candidates for that internal source.

We present here Ultra-High-Resolution observations of these stable components in the Ca II line of β Pictoris, gathered between 1993 and 1996. The observations are presented in Sect. 2, leading to a revised picture of the stable component. The consequences of this new fact on the model are discussed in Sect. 3.

As briefly mentioned in Lagrange et al. (1998), we show that our observations lead us to identify a new kind of variable feature, that is discussed in Sect. 4. We show that they may also be interpreted in the frame of the FEB scenario. We derive in Sect. 5 from these observations some constraints on the dynamical mechanism responsible for the FEB phenomenon. Our conclusions are presented in Sect. 6.

Send offprint requests to: H. Beust

⋆ Based on observations collected with the Ultra-High-Resolution Facility (UHRF) at the Anglo-Australian Telescope

Correspondence to: beust@obs.ujf-grenoble.fr

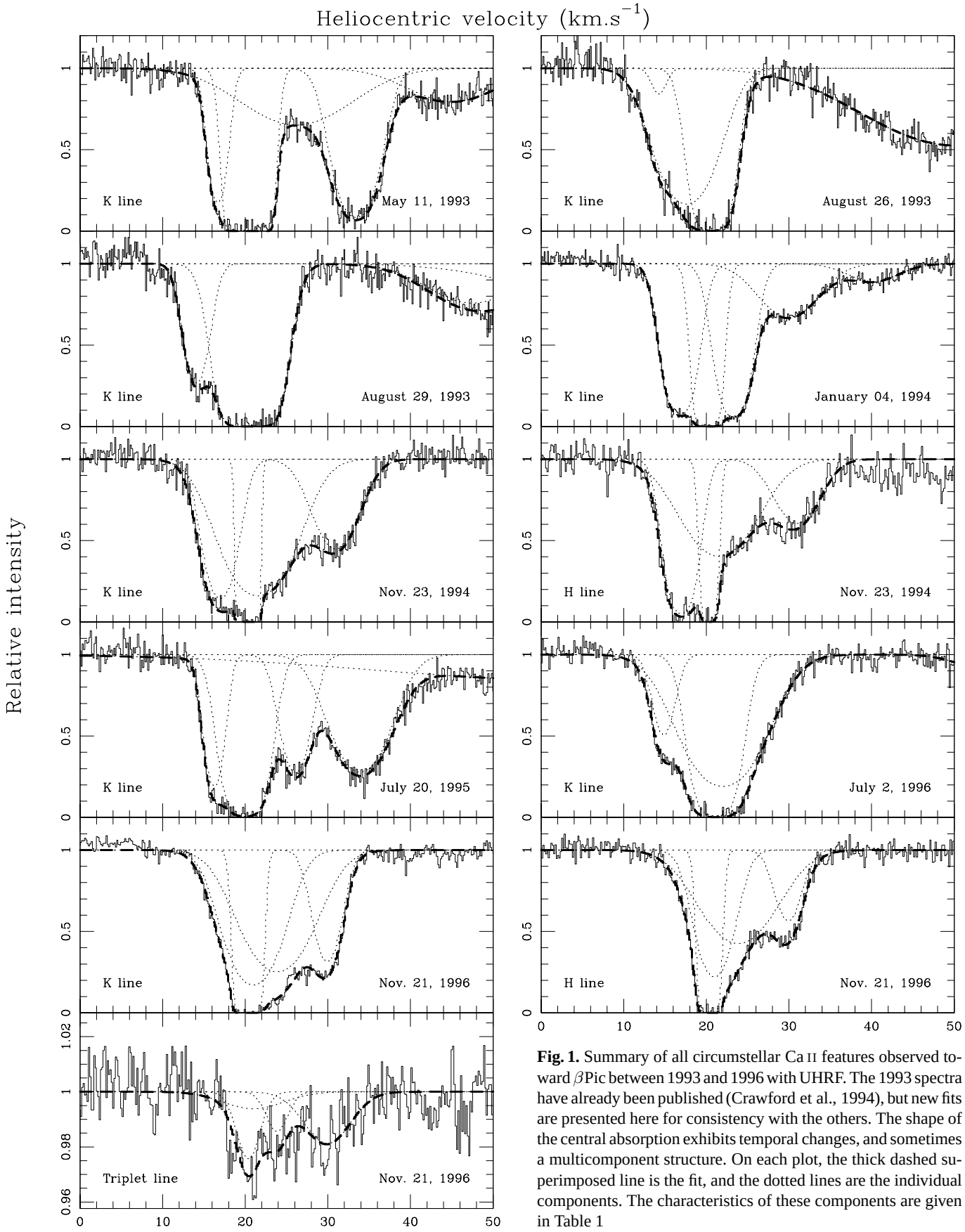

Fig. 1. Summary of all circumstellar Ca II features observed toward βPic between 1993 and 1996 with UHRF. The 1993 spectra have already been published (Crawford et al., 1994), but new fits are presented here for consistency with the others. The shape of the central absorption exhibits temporal changes, and sometimes a multicomponent structure. On each plot, the thick dashed superimposed line is the fit, and the dotted lines are the individual components. The characteristics of these components are given in Table 1

Table 1. Fitting parameters of the individual components found for all the available data. The uncertainties on the parameters were derived by the Levenberg-Marquardt method, assuming a global uncertainty of 0.1 on the relative depths in the data. The grey highlighted columns corresponds to the actual "central" component. Note that for the November 21, 1996 data, two equally accurate solutions were found. In Fig. 1, only the first one is displayed

Date	Parameter	Component #1	Component #2	Component #3	Component #4	Component #5
May 11, 1993	FWHM, K line ($\mathrm{km\,s^{-1}}$)	2.29 ± 0.76	2.91 ± 0.45	14.37 ± 3.79	4.93 ± 0.41	12.15 ± 2.20
	$\log N$, K line ($\mathrm{cm^{-2}}$)	11.80 ± 0.39	13.30 ± 0.39	11.99 ± 0.12	12.29 ± 0.05	11.65 ± 0.10
	v, heliocentric ($\mathrm{km\,s^{-1}}$)	16.69 ± 0.84	20.43 ± 0.38	26.20 ± 3.43	33.43 ± 0.10	45.11 ± 1.36
August 26, 1993	FWHM, K line ($\mathrm{km\,s^{-1}}$)	5.90 ± 1.12	4.26 ± 0.35	23.32 ± 0.87		
	$\log N$, K line ($\mathrm{cm^{-2}}$)	12.16 ± 0.20	12.57 ± 0.13	12.38 ± 0.01		
	v, heliocentric ($\mathrm{km\,s^{-1}}$)	16.36 ± 1.23	20.59 ± 0.39	50.31 ± 0.36		
August 29, 1993	FWHM, K line ($\mathrm{km\,s^{-1}}$)	3.11 ± 0.31	5.31 ± 0.28	11.92 ± 1.20	30.58 ± 1.90	
	$\log N$, K line ($\mathrm{cm^{-2}}$)	11.82 ± 0.06	12.86 ± 0.06	11.72 ± 0.06	12.47 ± 0.02	
	v, heliocentric ($\mathrm{km\,s^{-1}}$)	14.10 ± 0.21	20.59 ± 0.14	47.48 ± 0.50	75.21 ± 0.49	
January 04, 1994	FWHM, K line ($\mathrm{km\,s^{-1}}$)	3.72 ± 0.53	2.40 ± 1.69	3.79 ± 1.03	7.86 ± 2.12	7.02 ± 2.47
	$\log N$, K line ($\mathrm{cm^{-2}}$)	12.21 ± 0.14	12.50 ± 0.55	12.24 ± 0.23	11.71 ± 0.11	11.12 ± 0.16
	v, heliocentric ($\mathrm{km\,s^{-1}}$)	16.78 ± 0.57	20.13 ± 0.53	23.28 ± 0.88	29.95 ± 0.69	40.20 ± 1.19
November 23, 1994	FWHM, K line ($\mathrm{km\,s^{-1}}$)	3.87 ± 0.48	1.08 ± 0.94	8.43 ± 0.69	5.87 ± 0.49	
	FWHM, H line ($\mathrm{km\,s^{-1}}$)	3.45 ± 0.39	1.50 ± 0.37	9.41 ± 0.86	5.95 ± 0.59	
	$\log N$, K line ($\mathrm{cm^{-2}}$)	12.08 ± 0.10	13.96 ± 4.48	12.39 ± 0.05	11.88 ± 0.05	
	$\log N$, H line ($\mathrm{cm^{-2}}$)	11.98 ± 0.06	12.44 ± 0.04	12.47 ± 0.29	12.51 ± 0.07	
	v, heliocentric ($\mathrm{km\,s^{-1}}$)	16.98 ± 0.23	20.34 ± 0.14	21.55 ± 0.48	30.97 ± 0.28	
July 20, 1995	FWHM, K line ($\mathrm{km\,s^{-1}}$)	2.41 ± 0.64	4.31 ± 1.04	3.66 ± 0.57	7.19 ± 0.40	55.31 ± 5.98
	$\log N$, K line ($\mathrm{cm^{-2}}$)	11.80 ± 0.37	12.53 ± 0.11	11.88 ± 0.07	12.17 ± 0.02	12.18 ± 0.04
	v, heliocentric ($\mathrm{km\,s^{-1}}$)	16.25 ± 0.58	20.00 ± 0.53	26.07 ± 0.26	33.91 ± 0.17	60.01 ± 2.12
July 2, 1996	FWHM, K line ($\mathrm{km\,s^{-1}}$)	2.88 ± 0.74	4.49 ± 0.97	9.59 ± 0.65	9.18 ± 1.58	
	$\log N$ ($\mathrm{cm^{-2}}$)	11.50 ± 0.21	12.51 ± 0.17	12.41 ± 0.12	11.28 ± 0.07	
	v, heliocentric ($\mathrm{km\,s^{-1}}$)	14.86 ± 0.31	21.09 ± 0.25	22.01 ± 0.68	55.51 ± 0.68	
November 21, 1996	FWHM, K line ($\mathrm{km\,s^{-1}}$)	1.84 ± 0.27	6.62 ± 0.33	8.69 ± 0.53	3.52 ± 0.16	
	FWHM, H line($\mathrm{km\,s^{-1}}$)	1.70 ± 0.20	4.53 ± 0.36	9.61 ± 0.33	3.49 ± 0.21	
	FWHM, triplet line ($\mathrm{km\,s^{-1}}$)	3.36 ± 4.23	8.58 ± 33.52	3.05 ± 3.00	6.54 ± 3.38	
	$\log N$, K line ($\mathrm{cm^{-2}}$)	12.88 ± 0.37	12.27 ± 0.06	12.28 ± 0.07	11.81 ± 0.04	
	$\log N$, H line ($\mathrm{cm^{-2}}$)	12.79 ± 0.18	12.34 ± 0.04	12.42 ± 0.03	11.80 ± 0.05	
	$\log N$, triplet line ($\mathrm{cm^{-2}}$)	10.73 ± 1.53	10.54 ± 2.87	10.46 ± 0.93	10.91 ± 0.21	
	v, heliocentric ($\mathrm{km\,s^{-1}}$)	20.37 ± 0.06	20.99 ± 0.11	23.86 ± 0.29	29.94 ± 0.05	
November 21, 1996	FWHM, K line ($\mathrm{km\,s^{-1}}$)	4.90 ± 1.26	1.96 ± 0.26	7.37 ± 0.48	4.02 ± 0.10	
(second solution)	FWHM, H line($\mathrm{km\,s^{-1}}$)	6.37 ± 5.64	2.19 ± 0.13	7.11 ± 0.47	4.24 ± 0.12	
	FWHM, triplet line ($\mathrm{km\,s^{-1}}$)	0.92 ± 1.02	1.77 ± 1.86	6.31 ± 3.49	6.93 ± 3.55	
	$\log N$, K line ($\mathrm{cm^{-2}}$)	11.26 ± 0.60	12.85 ± 0.32	12.52 ± 0.04	11.95 ± 0.02	
	$\log N$, H line ($\mathrm{cm^{-2}}$)	10.76 ± 1.97	12.64 ± 0.07	12.54 ± 0.04	12.03 ± 0.02	
	$\log N$, triplet line ($\mathrm{cm^{-2}}$)	10.11 ± 0.49	10.33 ± 0.49	10.91 ± 0.27	10.91 ± 0.21	
	v, heliocentric ($\mathrm{km\,s^{-1}}$)	18.22 ± 0.39	20.43 ± 0.04	22.23 ± 0.31	29.65 ± 0.07	

2. Observations

2.1. Journal of observations and line parameters

Ultra high resolution ($R = 10^6$) spectra have been obtained since three years at the Anglo-Australian Telescope with the UHRF spectrometer. The spectrograph is described in detail in Diego et al. (1995). The reduction reduction procedure may be found in Crawford et al. (1994, 1998). All the gathered Ca II K data are diplayed on Fig. 1.

As already mentioned in Lagrange et al. (1998), the stable Ca II K (previously termed "central") components exhibit at a resolution of $R = 10^6$ composite structures with several blended components within $\pm 10\,\mathrm{km\,s^{-1}}$ around the stellar radial velocity. To separate them, we performed profile fitting on these lines, each individual component being characterized by three independent parameters: its helocientric velocity v, its FWHM, and the column density N of absorbing material. The numerical method is the Levenberg-Marquardt χ^2-minimizing algorithm. When only Ca II K lines are available at one epoch, we fix a number of components and adjust Voigt profiles to fit the data. When Ca II K and Ca II H spectra are available simultaneously, we fit both lines at the same time, forcing the velocities of the components to be the same in both lines. Whenever Calcium triplet (λ8542 Å) data are also available, simultaneously with the Ca II K and H data, the same strategy is adopted, thus combining the three lines.

The results are shown in Fig. 1, where the fitted profiles are superimposed to the original data. The characteristics of the individual components are listed in Table 1. Up to five distinct components are sometimes required to properly fit the data. We note that most of these components concentrate within $\pm 10\,\mathrm{km\,s^{-1}}$ around the radial velocity of the star ($20\,\mathrm{km\,s^{-1}}$), and that their typical FWHM is $\sim 5\,\mathrm{km\,s^{-1}}$. We also note that on each spectrum, a peculiar component may be found, usually the closest one to the radial velcity of the star, that is clearly deeper ($\log N$ values reaching sometimes almost 14) and narrower (FWHM between 1 and $3\,\mathrm{km\,s^{-1}}$) than the other ones. This is particularly obvious in the Nov. 23, 1994, and Nov. 21, 1996 data, where the deepest components clearly appears narrower than the other ones. We will thus define this component as the actual "central" (stable) circumstellar component. The other components therefore present a slight red- or blue-shift with respect to the star, and that are subject to temporal variations, as it may be seen from Fig. 1. In Table 1, the columns corresponding to the central component have been highlighted in grey.

From Table 1, we note that the line profile characteristics of the "central" components are $1\,\mathrm{km\,s^{-1}} \lesssim \mathrm{FWHM} \lesssim 5\,\mathrm{km\,s^{-1}}$ and $12.5 \lesssim \log N \lesssim 14$. However, we think that the widest central components (namely those of Aug. 1993, July 1995 and July 1996) are still unresolved. The fitting program did not succeed in separating them into narrower components, but they are probably still blended with smaller components, so that we may estimate the actual constraint on the FWHM for the central component to $1\,\mathrm{km\,s^{-1}} \lesssim \mathrm{FWHM} \lesssim 3\,\mathrm{km\,s^{-1}}$.

3. Analysis of the stable component

As the actual stable component appears narrower than previously suggested by the CAT/CES data, it is necessary to revise the analysis we had already performed in previous papers (Mouillet & Lagrange, 1995; Lagrange et al., 1998).

3.1. Constraints deduced from the width of the stable line

The linewidth of the stable line actually depends on several parameters. If we assume, as described in Lagrange et al. (1998), that the stable component is generated by a radial gaseous flow, basically concentrated at a given stellar distance, the width of the resulting line may be affected by:

- the radial velocity profile within the flow;
- the kinetic temperature of the absorbing medium;
- the Keplerian enlargement, i.e., the non-zero projection of the azimuthal (assumed Keplerian) velocity of the outflowing gas, due to the non-zero size of the line of sight;
- an eventual dispersion (turbulent) velocity within the absorbing medium;
- the resolving power of the instrument.

If the Keplerian enlargement was only active, then we would have, for a gas ring located at stellar distance d:

$$\mathrm{FWHM} = 2\sqrt{\frac{GM_*}{d}}\frac{R_*}{d}\ , \qquad (1)$$

where M_* and R_* are respectively the mass and radius of the star. As other processes may broaden the lines, the actual FWHM is in any case larger than this value. Conversely, any FWHM estimate thus leads to a minimum value for d. If we assume FWHM=$2\,\mathrm{km\,s^{-1}}$, we derive $d > 0.36$A.U.. We may therefore conclude that the gas is located further away than this limit. This is in fact compatible with our previous estimate.

Similarly, if we assume the line-width to be dominated by the kinetic temperature only, then a FWHM equal to $2\,\mathrm{km\,s^{-1}}$ correspond (for Ca II) to a temperature of 3500 K. Again, as other processes enlarge the lines, we can conclude that the actual temperature of the stable gas is less than 3500 K.

3.2. Physical conditions in the medium, deduced from the triplet line analysis

We performed a similar analysis as done in Mouillet & Lagrange (1995), comparing the Ca II K and triplet lines obtained in November 1996 to derive constrains on the electronic densities N_e and temperature T_e of the medium. We revised however some numerical values necessary in the calculations: first the new value of the β Pictoris distance derived from Hipparcos data (Crifo et al., 1997), and also better estimates of the stellar flux, deduced from a combination of HST spectra and Kurucz models.

With the ratio of Calcium triplet to ground level found ($10^{-2.32^{+1.09}_{-1.05}}$), we find that $N_\mathrm{e} \times T_\mathrm{e} > 10^5 \mathrm{cm}^{-3} \times \mathrm{K}^{-1/2}$ for values of T_e ranging between 1000 and 10000 K. For small values of T_e, the distance is smaller than 15 AU, whereas the distance should be greater than 15 AU for values of 10000 K.

3.3. Modeling the stable gas

In Lagrange et al. (1998), we presented a hydrodynamical model of the stable gas, based on HST-GHRS spectroscopic data of Ca II, but also Fe II, Si II and other species. We showed that the data could be satisfactorily reproduced assuming an internal source for the metallic ions, and that once blown away by the intense radiation pressure, the ions are stopped by a ring of neutral material (mainly H I) located somewhat further away from the star (0.5 A.U.). This study also showed that the various lines are correctly fitted with an additional dispersion velocity $v_\mathrm{disp} \simeq 2\,\mathrm{km\,s^{-1}}$, and an excitation/kinetic temperature of $T \simeq 2000$ K.

The present UHRF data shows that the actual central component in Ca II lines is narrower than previously assumed. Hence we now check whether the model developed in Lagrange et al. (1998) is still compatible with these data. We then apply this model, letting the various parameters vary, namely v_disp, T, the production rate Q of ionic material, and the location of the H I ring. The empiric H I density profile assumed (see Lagrange et al., 1998, for details) is (r is the distance to the star):

$$n(r) = A\left(\frac{r_\mathrm{m}}{r}\right)^x \exp\left[\frac{x}{y}\left(1-\left(\frac{r_\mathrm{m}}{r}\right)^y\right)\right]\ , \qquad (2)$$

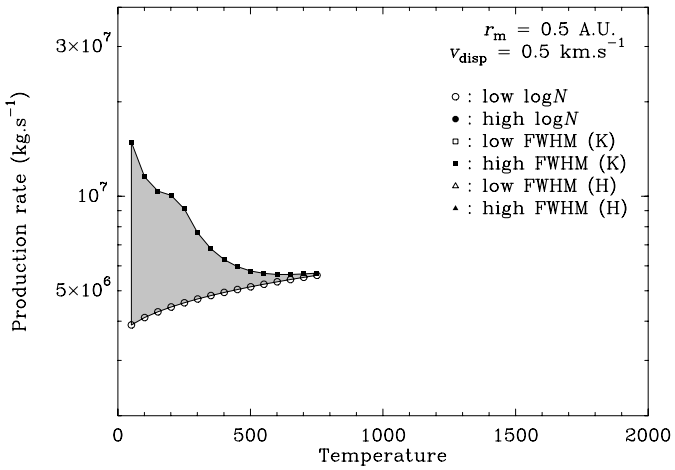

Fig. 2. Simulation output for Ca II circumstellar lines, with a H I ring located at $r_{\rm m} = 0.5$ AU from the star. We plot here in a (Q, T) plane (in grey) the parameter zone where the computed Ca II K and H lines fit into the $\log N$ and FWHM boundary constraints. The velocity dispersion $v_{\rm disp}$ is fixed to $0\,{\rm km\,s^{-1}}$. The symbols at the edges of the suitable zone indicate the reason why the suitable zone end up here: open circles indicate a boundary due to a too low $\log N$, and filled circles correspond to a too high $\log N$. Open squares and filled squares indicate similarly a too low and too high FWHM, respectively

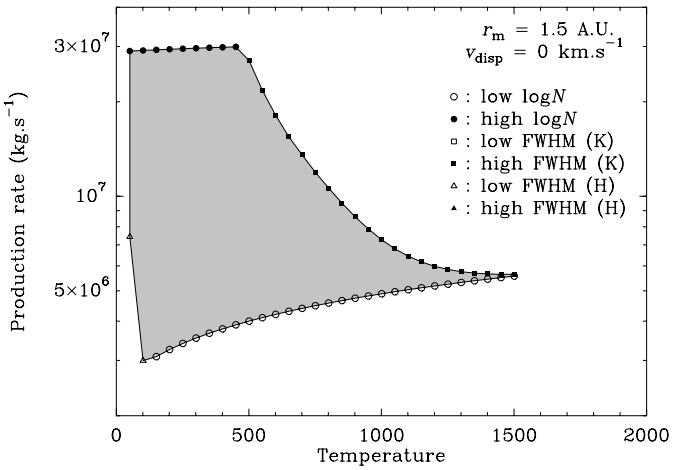

Fig. 3. Same as Fig. 2, but for $r_{\rm m} = 1.5\,{\rm AU}$

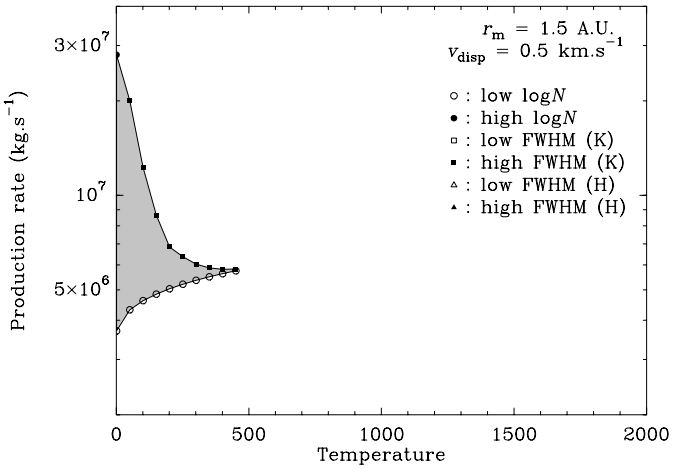

Fig. 4. Same as Fig. 2, but for $r_{\rm m} = 1.5\,{\rm AU}$ and $v_{\rm disp} = 0.5\,{\rm km\,s^{-1}}$

where A, $r_{\rm m}$, x and y are adjustable parameters. This profile is well suited to simulate a ring-like distribution. Basically, $r_{\rm m}$ is the location of the density peak of the ring, x and y are exponents characterizing the steepness of the decrease outside the peak, and A is a scaling factor. In Lagrange et al. (1998), we showed that changing the values of x and y does not have a strong effect on the resulting circumstellar lines, provided the value of A is adjusted in order to keep the total column density $N(H)$ unchanged (roughly, we have $N(H) \propto A \times r_{\rm m}$). We will then assume in the following the same values as in Lagrange et al. (1998), namely $x = 9$ and $y = 3$. We let $r_{\rm m}$ vary, but changing A in order to keep the $N(H)$ value ($\sim 8\,10^{18}\,{\rm cm^{-2}}$) constant; this is the value assumed in Lagrange et al. (1998), and it is compatible with the observational constraints (Lagrange et al., 1995; Freudling et al., 1995).

We first adopt the H I distribution assumed in Lagrange et al. (1998), i.e., with $r_{\rm m} = 0.5\,{\rm AU}$. The result is shown on Fig. 2, for $v_{\rm disp} = 0\,{\rm km\,s^{-1}}$, where the zone where the constraints are satisfied is drawn in a (Q, T) plane. We note that the production rate (Q) value is still compatible (although slightly smaller) with the one deduced in Lagrange et al. (1998) ($1.3\,10^7{\rm kg\,s^{-1}}$, for Ca II data). We note also that, conversely to the results obtained in Lagrange et al. (1998) from the comparison of Fe II lines, the temperature is here constrained to less than 500 K. The present results are valid for $v_{\rm disp} = 0\,{\rm km\,s^{-1}}$. We did the same calculations with $v_{\rm disp} = 0.5$ and $1\,{\rm km\,s^{-1}}$. In those cases, *no* acceptable zone in the (Q, T) plane was found.

We thus performed the same calculations for $r_{\rm m} = 1.5\,{\rm AU}$ (scaling A in order to keep $\log N$ constant). The result is shown on Figs. 3 and 4, for $v_{\rm disp} = 0$ and $0.5\,{\rm km\,s^{-1}}$ respectively. We see that the suitable zones are larger. For $v_{\rm disp} = 1\,{\rm km\,s^{-1}}$, there is still no acceptable zone.

The behavior difference between $r_{\rm m} = 0.5\,{\rm AU}$ and $r_{\rm m} = 1.5\,{\rm AU}$ is only due to the Keplerian enlargement: at large distances, the Keplerian enlargement is smaller, so that the FWHMs of the resulting lines are globally smaller, leading to a weaker constraint on the parameters. We also tried larger stellar distances (namely $r_{\rm m} = 4\,{\rm AU}$), but at such a distance, the difference with respect to $r_{\rm m} = 1.5\,{\rm AU}$ appears to be small. At large enough distances, the Keplerian enlargement becomes negligible, so that changing the location of the H I ring does not affect the lines.

The first conclusion we may draw from this study is that there is here a discrepancy concerning the temperature and dispersion velocity values between the present results and those of Lagrange et al. (1998). We note however that the values deduced in Lagrange et al. (1998) were based on the relative depths of Fe II lines, and that the present discussion deals with line-widths. These parameters might not be coupled. The *kinetic* temperature might for example not coincide with the *excitation*

temperature, if thermal equilibrium is not achieved. We note however that the production rate (Q) values obtained are compatible with those deduced in Lagrange et al. (1998). Basically, the main discrepancy concerns the dispersion velocity which is better constrained by the present data.

It also seems that the data are better reproduced if we assume the H I ring to be somewhat further away from the star than assumed in Lagrange et al. (1998) (1.5 AU or more instead of 0.5 AU). In fact, the only observational constraint on this value are the Ca II triplet measurements (see above), which give $r_{\rm m} \lesssim 15$ AU. Nevertheless, if we believe that the H I ring is produced and replenished by comets, we may stress that it must be located inside the evaporation zone for water ice. Considering large icy particles (size $\gtrsim 1\,\mu$m), this gives $r_{\rm m} \lesssim 5$ AU (see below, Fig. 5), a stronger constraint, but still compatible with the data.

4. The very low velocity variable lines

4.1. General features

The analysis of the stable Ca II component with UHRF reveals that apart from the narrow stable component, a few transient very low velocity components (less that 10 km s^{-1} with respect to the bottom of the stable component) are present. All these components are blended in the CAT/CES data (at $R \simeq 10^5$) with the central one. They are time-variable in shapes, number and velocities (see Table 1). Hence, we may link them with the variable spectral events observed now for many years at higher redshifts.

More specifically, the variable features observed up to now at lower resolution were divided into two distinct classes: Low velocity features (hereafter LVFs), and High velocity features (hereafter HVFs). LVFs are the most frequently observed, they are usually deep (typically 50% of the continuum), their redshift velocity with respect to the central component ranges between 10–20 and 50 km s^{-1}, and their FWHM peaks around $\sim$ 11 km s^{-1} (see Lagrange et al., 1996). Some blueshifted LVFs were recorded by Crawford et al. (1998), and also marginally by Bruhweiler et al. (1991), but they are far less numerous than redshifted ones, and should therefore regarded as outliers from the main distribution.

In contrast with LVFs, HVFs are not very deep (10% of the continuum at most), they present higher redshifts (typically 100 km s^{-1}), and their FWHM is much larger (typically 30 km s^{-1}). HVFs also appear to vary on shorter time-scales than LVFs. All these characteristics are naturally interpreted and reproduced in the frame of the FEB scenario, HVFs corresponding to FEBs crossing the line of sight at smaller stellar distances (typically $\lesssim$ 8–10 R_*) than LVFs (Beust et al., 1996).

The new very low velocity features (hereafter VLVFs) revealed by the UHRF data (Table 1) are quite distinct from both the LVFs and the HVFs, as their velocities range from -10 to 10 km s^{-1}, and that their FWHM is typically 5 km s^{-1}. Note that in Table 1, some of the identified components, namely those having the largest redshift velocities, actually correspond to "regular" LVFs, with a large FWHM. The VLVFs are nevertheless as deep, and even deeper than the LVFs and may vary on similar time-scales. We note also that they verify the general trend noted in Lagrange et al. (1996) that the FWHM of the variable lines is an increasing function of the redshift velocity. It is thus legitimate to wonder whether these new features might also be explained in the frame of the FEB model.

4.2. Grain evaporation at large distances

According to the FEB phenomenon, lower redshifts and smaller FWHMs correspond to bodies crossing the line of sight at larger distances from the star. As described in Beust et al. (1996), the redshift velocity of a given component is directly linked to the projection velocity of the passing FEB onto the line of sight, which is larger when closer to the star. The variation of the FWHM is less straightforward, but when the body is close enough to the star, it is dominated by the rotation of the coma, following the frame of the nucleus. These assumptions lead (see Beust et al., 1996) to $\mathrm{FWHM} \propto d^{-5/6}$ and $\mathrm{FWHM} \propto v^{5/3}$ (d is the stellar distance and v is the redshift velocity).

Hence we might suppose that the VLVFs are due to bodies evaporating somewhat further away from the star than LVFs. However, these bodies need to be close enough to the star in order to allow refractory grain bearing species like calcium or iron to evaporate. In Beust et al. (1996), we presented a rough analysis of grain evaporation based on black-body assumptions, leading to an evaporation limit around $35\,R_*$. This simple model cannot appear satisfactory here, as we want to consider the evaporation of bodies close to this limit. Hence we want to use a more realistic model for grain evaporation.

4.2.1. Theoretical background

Dust evaporation depends on the equilibrium temperature reached by individual grains. The basic equation determining the equilibrium temperature of a given (evaporating) grain is (Lamy, 1974)

$$E_{\rm star} = E_{\rm rad} + E_{\rm subl} \quad , \tag{3}$$

where $E_{\rm star}$ stands for the energy received from the stellar radiation, $E_{\rm rad}$ is the energy radiated by the grain, and $E_{\rm subl}$ is the energy used for sublimating material. As noted by Lien (1990), other sources like the interaction with a stellar wind, a collisional heating by the gas, or the nucleus radiation, are negligible. Assuming a spherical grain of radius s, located at distance d from the star, we have

$$E_{\rm star} = \left(\frac{\Omega}{\pi}\right) \pi s^2 \int_0^{+\infty} Q_{\rm abs}(s,\lambda)\, F_*(\lambda)\, {\rm d}\lambda \; ; \tag{4}$$

$$E_{\rm rad} = 4\pi s^2 \int_0^{+\infty} Q_{\rm abs}(s,\lambda) B(\lambda,T)\, {\rm d}\lambda \; ; \tag{5}$$

$$E_{\rm subl} = 4\pi s^2 \frac{{\rm d}E}{{\rm d}t} L_{\rm s}(T) \; , \tag{6}$$

where T is the equilibrium temperature of the grain, ${\rm d}E/{\rm d}t$ and $L_{\rm s}(T)$ are respectively the mass sublimation rate (per unit of surface) and the latent heat of sublimation at temperature T, $F_*(\lambda)$

is the monochromatic flux of the star, $B(\lambda, T)$ is Planck's function at temperature T, $Q_{\rm abs}(s, \lambda)$ is the absorption efficiency of the grain, and Ω is the solid angle subtended by the star at distance d. We have

$$\Omega = 2\pi \left(1 - \sqrt{1 - \left(\frac{R_*}{d} \right)^2} \right) \ . \tag{7}$$

Whenever $d \gtrsim R_*$, $\Omega \simeq \pi \left(R_*/d \right)^2$. The mass sublimation rate may be expressed as (Lamy, 1974)

$$\frac{{\rm d}E}{{\rm d}t} = \alpha p(T) \sqrt{\frac{m}{2\pi kT}} \quad , \tag{8}$$

where $p(T)$ is the vapor pressure, k is Boltzmann's constant, m is the molecular weight of the evaporating material, and α is an efficiency factor we assume equal to 0.7 (Lamy, 1974).

Evaluating T for a given grain located at distance d from the star thus requires the knowledge of

- the emission flux of the star $F_*(\lambda)$;
- the absorption efficiency $Q_{\rm abs}(s, \lambda)$;
- the latent heat $L_{\rm s}(T)$ and the vapor pressure $p(T)$.

We used for the stellar flux a Kurucz model (Kurucz, 1979) between $\lambda = 1250$ Å and $\lambda = 10000$ Å with a 0.03 Å step, with $T_{\rm eff} = 8200$ K and $\log g = 4.25$, according the recent Hipparcos based measurements by Crifo et al. (1997). In order to calibrate this spectrum, we used the HST/GHRS spectroscopic data between 2000 and 3000 Å presented in Lagrange et al. (1998). At wavelength larger than 10000 Å the spectrum was extrapolated using a Planck function.

The absorption efficiency $Q_{\rm abs}(s, \lambda)$ is obtained from the Mie theory (Bohren & Huffmann, 1983). It depends on of the optical properties (dielectric constants) of the considered material. The latent heat of sublimation is related to the vapor pressure through the Clausius-Clapeyron equation (Leger et al., 1983):

$$\ln p = -\frac{mL_{\rm s}}{kT} + b(T) \ , \tag{9}$$

where $b(T)$ is a constant of integration. They are also function of the evaporating material.

Once the equilibrium temperature is obtained, the lifetime of the grain versus sublimation may be expressed as

$$t_{\rm life} = \frac{s}{|{\rm d}s/{\rm d}t|} = \frac{s\delta}{{\rm d}E/{\rm d}t} = \frac{s\delta}{\alpha p(T)} \sqrt{\frac{2\pi kT}{m}} \ , \tag{10}$$

where δ is the density of the material.

4.3. Various materials

We calculated lifetimes of grains made of various materials, refractory ones as well as volatiles. As typical refractory materials, we considered obsidian, graphite, magnetite and amorphous carbon. For volatiles, we considered water ice and CO_2 ice. For obsidian, we used the optical constants for the so-called "astronomical silicates" of

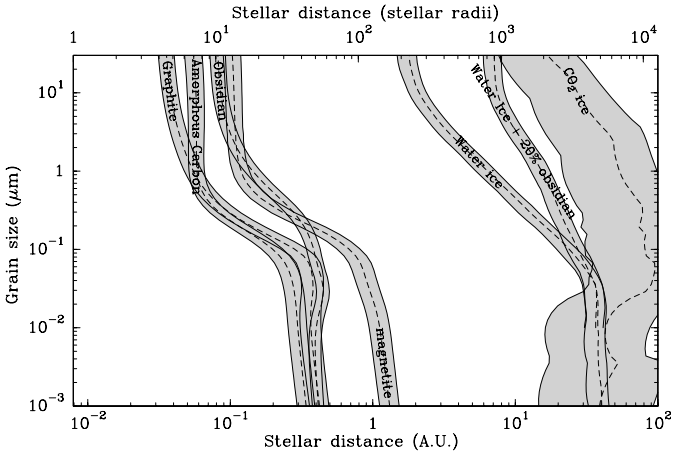

Fig. 5. Sublimation regions for various materials. For each material, the main sublimation region is delimited by a grey zone: the inner edge of the zone corresponds to the distance where $t_{\rm life} = 0.1$ day, while the outer edge corresponds to $t_{\rm life} = 10$ days. The dashed line indicates $t_{\rm life} = 1$ day. Most of the sublimation is thus expected to occur within the grey zone

Draine & Lee (1984), revised in Laor & Draine (1993); the same references were used for graphite. Magnetite (Fe_3O_4) data were taken from Henning et al. (1995), amorphous carbon data from Zubko et al. (1996), water ice data from Warren (1984) and CO_2 ice from Warren (1986). Vapor pressure formulæ, latent heats for sublimation and densities are listed in Table 2.

We also calculated dirty-ice models, i.e. icy spheres contaminated by silicates in the form of small inclusions. If the inclusions occupy a volume fraction $f \ll 1$ of the grain, and have a dielectric constance ϵ, while $\epsilon_{\rm m}$ is that of the matrix, then the average dielectric function of the grain is given by the Maxwell-Garnett theory (Maxwell-Garnett, 1904):

$$\overline{\epsilon} = \epsilon_{\rm m} \left(1 + \frac{3fq}{1 - fq} \right) \ , \qquad \text{with} \qquad q = \frac{\epsilon - \epsilon_{\rm m}}{\epsilon + 2\epsilon_{\rm m}} \tag{11}$$

The vapor pressure and the latent heat for sublimation will be assumed to be that of the matrix.

4.3.1. Results

The results of sublimation calculations for various materials are summarized in Fig. 5. In this plot, the sublimation limiting region for each material (defined as the region where $0.1\,{\rm day} < t_{\rm life} < 10\,{\rm days}$) is sketched as a grey zone. Note that these results may be affected by the radiation pressure, as for particles around 0.1μm, the radiation pressure may be strong enough (Artymowicz, 1988) to blow them away before they evaporate. This is of course only valid where $t_{\rm life}$ is large enough ($\gtrsim 1$ day). However, considering that the dusty particles under consideration are produced near a cometary-like nucleus in a fairly dense medium, it turns out that they first have to slightly expand away radially from the nucleus before being blown away by the radiation pressure. Hence they may evaporate before the radiation pressure acts on them.

Table 2. Sublimation parameters assumed for various materials

Material	Molecular weight (a.m.u.)	Density ($\mathrm{g\,cm^{-3}}$)	Vapor pressure (Torr) (T in Kelvins)	Latent heat for sublimation ($\times 10^6\,\mathrm{J\,kg^{-1}}$)	Reference
Obsidian	67	2.37	$\log p = 10.915 - 24928.3/T$	7.079	Lamy (1974)
Magnetite	232	5.20	$\log p = 16.89 - 21080/T - 2.14 \log T$ [a]	1.739	Lamy (1974) Mukai & Schwehm (1981)
Amorphous carbon	12	1.80	$\log p = 9.3813 - 27240/(T-9)$	43.452	Dean (1985)
Graphite	12	2.26	$\log p = 11.0428 - 37736/(T+29.2)$	60.195	Dean (1985)
Water ice	18	0.92	$\log p = -6.757 - 2445.6/T + 8.23 \log T - 0.01677\,T + 1.205\,10^{-5} T^2$ [b]	2.600	Lamy (1974)
			$\log p = 1.207 - 2461/T + 3.857 \log T - 3.41\,10^{-3}\,T + 4.875\,10^{-8}/T^2$ [c]	2.171	
CO_2 ice	44	1.35	$\log p = 9.81066 - 1347.786/T$	0.586	Dean (1985)

[a] Iron data assumed [b] for $T < 100\,\mathrm{K}$ [c] for $T > 100\,\mathrm{K}$

The first obvious conclusion is that there is a clear distinction between refractory compounds and volatiles, the latter ones sublimating at much larger distances from the star than the first ones. Another general trend is that for any given material (especially for refractory materials) we clearly identify two sublimation regimes, depending on the size of the grain: grains smaller than $\lesssim 0.1\,\mu$m begin to evaporate at somewhat larger distances from the star (~ 0.5 A.U, even further away for magnetite), while grains larger than $\sim 0.4\,\mu$m only evaporate around 0.1 A.U. Basically, this behavior may be understood as follows: most of the star's light is concentrated in the visible-close UV spectral region. For a large enough grain, most of the absorbed or scattered light will thus be in the frame the geometrical optics regime, characterized by $\mathrm{size} \gg \mathrm{wavelength}$. Conversely, very small grains will essentially encounter stellar light with $\mathrm{size} \ll \mathrm{wavelength}$, i.e. in the Rayleigh-Gans asymptotic regime. Hence, the turn-off point between these two extreme regimes just corresponds to sizes falling (in terms of wavelength) into the peak of spectral stellar emission.

We may also note that all the refractory materials present similar sublimation behaviors. In particular (apart from magnetite), the smaller grains begin to all evaporate in the same region. We may therefore stress that the sublimation characteristics of refractory dust grains involved on the FEB scenario should not drastically depend on the exact composition of the dust. In the following simulations, we will assume obsidian grains, keeping in mind that other materials behave similarly.

4.4. The revised FEB scenario

4.4.1. Changes to the model

We included the preceding results for dust sublimation into our simulation code dedicated to the FEB scenario, already described in Beust et al. (1990, 1991a, 1996). As the sublimation process depends on the size of the grains, we had to assume a size distribution. We assumed the very common following distribution function (Festou et al., 1993):

$$n(s)\,\mathrm{d}s = C \left(1 - \frac{s_{\min}}{s}\right)^M \left(\frac{s_{\min}}{s}\right)^N \quad , \qquad (12)$$

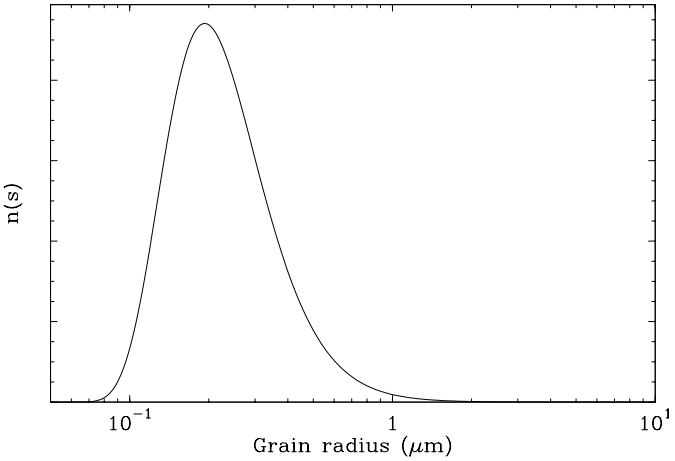

Fig. 6. Shape of the grain size distribution assumed

where s is the radius of the grain, $s_{\min}$ a cut-off radius value, and N and M are characteristic indexes. According to Festou et al. (1993), typical comet parameters are $0.02\,\mu\mathrm{m} < s_{\min} < 0.2\,\mu\mathrm{m}$, $3.5 < N < 4.6$ and $4 < M < 20$. We assumed $s_{\min} = 0.05\,\mu$m, $N = 4.2$ and $M = 12$, which are values quoted by Orosei et al. (1995). The corresponding size distribution is plotted on Fig. 6. This distribution peaks around $s = 0.2\,\mu$m.

It first appears from the simulations that the outer limit in order to observe spectral Ca II features from a passing FEB is ~ 45–$50\,R_*$, i.e. 0.35–0.4 A.U. At larger distances, dusty particles do not evaporate sufficiently before being blown away from the cometary coma by the radiation pressure, and no net line is to be expected in absorption. Note that the radiation pressure on dusty particles is also obtained by the Mie theory, and that it overcomes the stellar gravity as soon as $s \lesssim 1\,\mu$m. The same results were also obtained some years ago by Artymowicz (1988).

It also appears that it is not easy to reproduce absorption events with FWHM $\lesssim 5\,\mathrm{km\,s^{-1}}$ was not easy, basically because we assume (as before) a constant outflow velocity of the gaseous medium around the coma $v_{\mathrm{e}} = 3\,\mathrm{km\,s^{-1}}$. Obviously, even if close to the star, the FWHM of a given component is

controlled by the rotation of the coma, it cannot be smaller than ∼twice the outflow velocity. Indeed, the minimum FWHM we were able to obtain with $v_e = 3\,\mathrm{km\,s^{-1}}$ is $\sim 10\,\mathrm{km\,s^{-1}}$.

It is nevertheless worth recalling that the $v_e = 3\,\mathrm{km\,s^{-1}}$ value was an assumed average (Beust et al., 1996) between measured values close to the nucleus, which are close to $1\,\mathrm{km\,s^{-1}}$ (Lämmerzahl et al., 1987), and terminal expansion velocities measured for hydrogen in the outer coma (Bertaux et al., 1993). Assuming a gradual increase of v_e from the inner to the outer coma would indeed be a more realistic model than a simple constant value. This is why we assume now the theoretical outflow velocity curves for various gaseous species given by Hodges (1990), incorporating them into the simulation.

4.4.2. Simulation results

Figs. 7–9 show three simulation outputs reproducing a HVF, a LVF and a VLVF respectively. Only the orbital characteristics (the periastron distance q and the longitude of periastron ϖ with respect to the line of sight) have been changed between these runs. The three FEBs pass at 6, 16 and $35\,R_*$ respectively. They have slightly different ϖ values ($47°$, $20°$ and $-1°$ respectively). As explained below (in Sect. 5), this difference is assumed in order to take into account the necessary change of ϖ that occurs between FEBs having various periastron distances. This is related to the dynamical mechanism that generates the FEB phenomenon and is thus model dependent, but as explained below, assuming a constant ϖ value leads to a much less satisfactory fit of the velocities of the various kinds of spectral events. More specifically, the $\varpi = 20°$ values for the LVF generating FEB was fixed according to the results of Beust et al. (1996) (that basically concerned LVFs), and the ϖ values for the other ones were fixed according to the prediction of our mean-motion resonance model (see below), with respect to that central value.

Conversely, the gaseous (z) and dust (Q) production rates of the FEBs are identical and mentioned on the plots. The mass dust/gas ratio inferred by these values is 0.3, and such an evaporation rate is compatible with the total evaporation of a 1 km sized body over a time-scale of the order of one week.

We thus see that VLVFs are quite naturally explained by the FEB scenario, without requiring additional physics. In fact, VLVFs appear as an extension of LVFs toward large stellar distances. Further away from the star, the only limitation is the dust evaporation capability, as depicted by Fig. 5. In fact, the generated VLVFs appear to be very faint for FEBs passing further away than $\sim 45\,R_*$,

Deep VLVFs like those fitted on Fig. 1 are difficult to generate with a single passing FEB, unless a significantly higher evaporation rate is assumed. This also applies to LVFs. In fact, as shown in Beust et al. (1996), very deep features (depth $\gtrsim 50\,\%$) are more easily produced assuming that more than one body may be present simultaneously in front of the line of sight. This conclusion is moreover strongly suggested by the fact that we fit several individual components (at different velocities) in the spectra (Fig. 1), thus showing that several FEBs may actually cross the line of sight simultaneously.

5. The orbit orientation problem

5.1. The fixed orientation and the origin of FEBs

Figs. 7–9 illustrate that, in the frame of the FEB scenario, the key parameter for separating the various kinds of observed features is the stellar distance of the FEB when crossing the line of sight. The radial velocity of the FEB with respect to the star is nevertheless also a crucial parameter, as it controls the redshift (or blueshift) velocity of the resulting component. These two kinematic parameters (stellar distance d and redshift velocity v) are of course related to the orbital parameters q and ϖ. In fact (see Beust et al., 1996), if e is the eccentricity of the FEB orbit, we have

$$v = \sqrt{\frac{GM_*}{d}}\,\frac{e\sin\varpi}{\sqrt{1+e\cos\varpi}} \tag{13}$$

The eccentricity of the FEBs is necessary close to 1. Their orbit cannot be circular otherwize they could not survive where they are observed. If they are assumed to originate from the 4:1 mean-motion resonance with a massive planet located at ~ 10 A.U. (see below), their semi-major axis is ~ 4 A.U.; as they need to enter the dust evaporation zone in order to be observed, they must have $q \lesssim 0.4$ A.U., which leads to $e \gtrsim 0.9$. Assuming $e \simeq 1$, Eq. (13) reduces to

$$v =\simeq \sqrt{\frac{2GM_*}{d}}\,\sin\frac{\varpi}{2} \times \mathrm{sign}\left(\cos\frac{\varpi}{2}\right) \tag{14}$$

It was stressed in previous work (Beust et al., 1990, 1996) that the observational statistics on LVFs and HVFs require the distribution of the orientations of the orbit of the FEBs (i.e., ϖ) to peak around a fixed value instead of being be randomly distributed. Basically, if the longitude of the periastron of the FEBs was randomly distributed, the redshift velocity of the LVFs would not concentrate in the specific range 10–50 $\mathrm{km\,s^{-1}}$. This is in fact illustrated by Eq. (14). Consider a typical LVF distance of $20\,R_*$. The corresponding free fall velocity $\sqrt{2GM_*/d}$ is $\sim 140\,\mathrm{km\,s^{-1}}$, so that if ϖ was randomly distributed, we would expect v to be randomly distributed between -140 and $+140\,\mathrm{km\,s^{-1}}$. If we are back to Eq. (13), even if we assume an eccentricity down to 0.8, the velocity should range between -85 and $+85\,\mathrm{km\,s^{-1}}$. In any case, we would observe as many *blueshifted* as *redshifted* events, which is clearly not the case. In fact, the observed range in compatible with $\varpi = 20° \pm 10°$.

The FEBs orbits thus appear to align around a common direction when approaching the star. This fact is obviously related to the dynamical process that generates the FEB phenomenon. Two distinct mechanisms were recently proposed: Levison et al. (1995) argued that secular resonances like the ν_6 one in the Solar System are very efficient for locally pumping up the eccentricity of particles, making sun-grazers of them. Beust & Morbidelli (1996) also showed that the 4:1 and eventually the 3:1 mean-motion resonances with a massive planet on

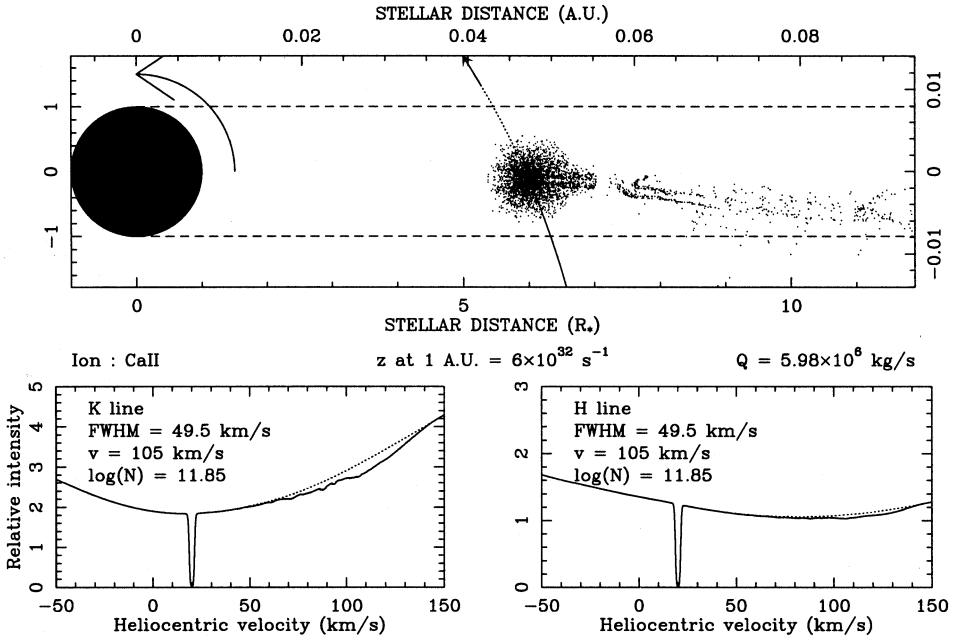

Fig. 7. Plot of a simulation reproducing a HVF, in both Ca II K and H lines. The upper plot shows a 2-D view of the Ca II cloud corresponding to the passing FEB, together with the star itself and a small part of the orbit. The line of sight is sketched as two parallel dashed lines. The lower plots show the synthetic Ca II K and H line profiles. In each plot, the dotted spectrum corresponds to the "quiet" profile when no FEB is present, while the other ones correspond to the simulated feature, together with the stable central (FWHM $= 1.7\,\mathrm{km\,s^{-1}}$) component. The fitting characteristics of the variable lines are indicated one the plots

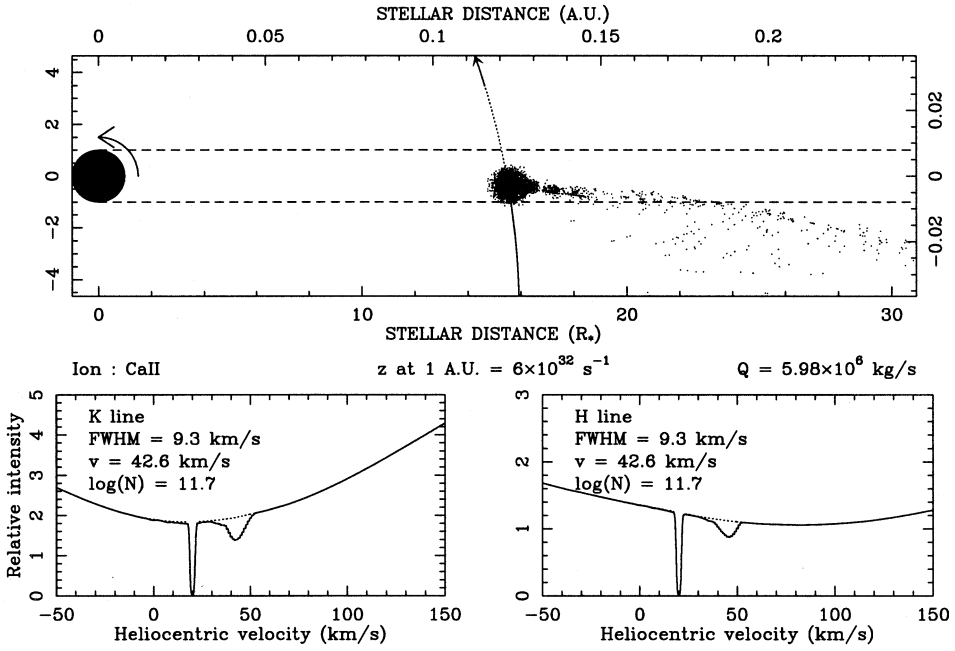

Fig. 8. Same as Fig. 7, but for a FEB passing at a larger distance to the star, and reproducing a LVF

a moderately eccentric orbit ($e' \gtrsim 0.05$) is also a strong source of star-grazers. Both models involve planetary perturbations, the first one requiring at least two planets, while the latter one only needs one. Both models predict a preferred orbit orientation of star-grazers, according to the observational constraints. However, the Levison et al. (1995) model has the disadvantage of being non-generic, as the ν_6 secular resonance is exceptionally strong in the Solar System (see Beust & Morbidelli, 1996).

Moreover, the latter model is the only one predicting a natural fluctuation of the rate of infall of the FEBs over a time-scale of a few years, as it seems to be observed (Beust et al., 1991b; Beust & Morbidelli, 1996). This fluctuation is due to the fact that the locations on their orbit of bodies trapped in a given mean-motion resonance with a planet (i.e., their mean longitude) are not randomly distributed, as they tend to avoid being in conjunction with the planet at apoastron (for an inner resonance; this corresponds to unstable equilibrium configurations), in order to minimize the perturbations effects. This may also be regarded as a consequence of the confinement of the critical argument of the resonance σ (see Beust & Morbidelli, 1996) induced by the libration that is characteristic for the mean-motion resonance dynamics. Consequently, a swarm of FEBs distributed on similar resonant orbits tend to pass at periastron at specific dates, depending of the location of the planet on its orbit. This leads to a natural fluctuation of the rate of FEB arrival, with a period equal to the fourth of the orbital period of the planet (for

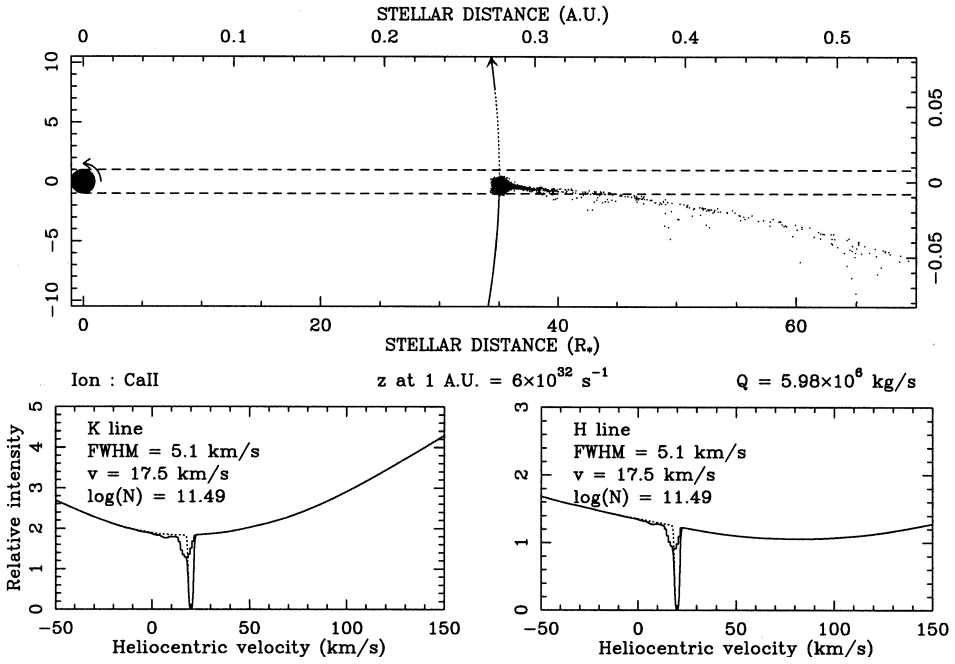

Fig. 9. Same as Fig. 7, but the FEB passes now much further away from the star, and produces a VLVF. Compared to Figs. 7 and 8, we have superimposed on the lower plots another spectrum showing the variable feature *without* the stable component. This makes the variable line appear better

the 4:1 resonance, of course). This may be easily numerically simulated, and corresponding runs will be presented in a forthcoming paper.

Conversely, the secular resonance model does not predict such a fluctuation over a typical time-scale of a few years, as the critical argument of such a resonance does not involve the mean longitudes, but angular orbital elements like longitudes of periastron and longitudes of the node (see e.g. Morbidelli & Moons, 1993, 1995). Hence the location on their orbits of FEBs trapped in a secular resonance is not constrained by the dynamics, contrary to the mean-motion resonant case.

For these reasons, the mean-motion resonance model will thus remain our preferred one.

5.2. VLVFs and the fixed direction hypothesis

We may now raise the question whether the fixed direction assumption for *all* FEBs is still compatible with the newly observed VLVFs. As suggested above, the answer is no. In order to lead to a correct fit of the observational velocities, it was necessary to assume slight changes of longitude of periastron between the three FEBs simulated in Figs. 7–9. It was shown that a random distribution for the longitude of periastra of the FEBs is not compatible with the observational constraints. One could argue however that if this is true for HVFs and LVFs, as these show up a strong trend towards redshifts with respect to blueshifts, this assumption may be questioned for VLVFs, whose velocity distribution is roughly symmetric around zero. However, even if it is symmetric, the width of this distribution ($\pm 10\,\mathrm{km\,s^{-1}}$) appears too narrow to be generated by randomly oriented orbits. Considering Eq. (14) with a maximum stellar distance $d = 40\,R_*$, demanding such a confined distribution requires $e \leq 0.14$, which is clearly unrealistic for survival purpose of the bodies.

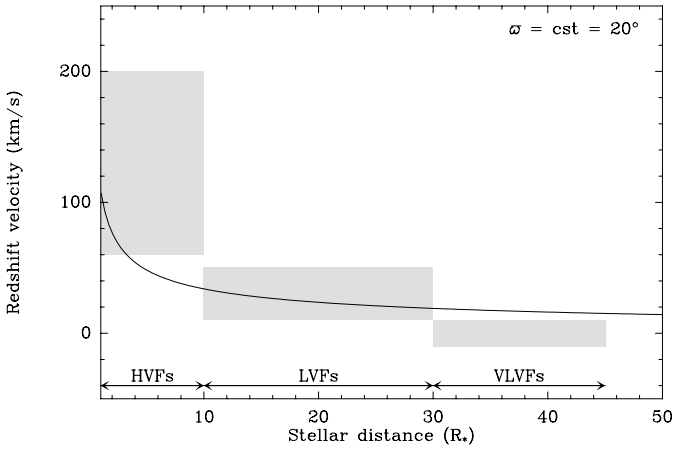

Fig. 10. Plot of the redshift velocity of passing FEBs as a function of stellar distance when crossing the line of sight, based on Eq. (14), for a constant longitude of periastron $\varpi = 20^\circ$. Only the LVF velocity range is correctly fitted. The grey boxes denote the constraints on the different features. Note that the borders of these zones are only approximate. The constraint in velocity is of course observational, but the borders in stellar distance between HVFs, LVFs and VLVFs are deduced from our model, i.e. simulations like those displayed in Figs. 7–9. This distinction is of course somewhat arbitrary and historical, but it is mainly based on the depths and shapes of the variable components that FEBs generate in the corresponding regions. These borders may therefore be considered accurate to ∼20–30 %

Hence, *for a given periastron distance*, or a given periastron range, we may stress that ϖ is strongly constrained around a fixed value. However, me may now suggest that this fixed value might be different for FEBs having a *different* periastron distance. In others words, the longitude of periastron would be a non-constant function of the periastron distance of the FEBs.

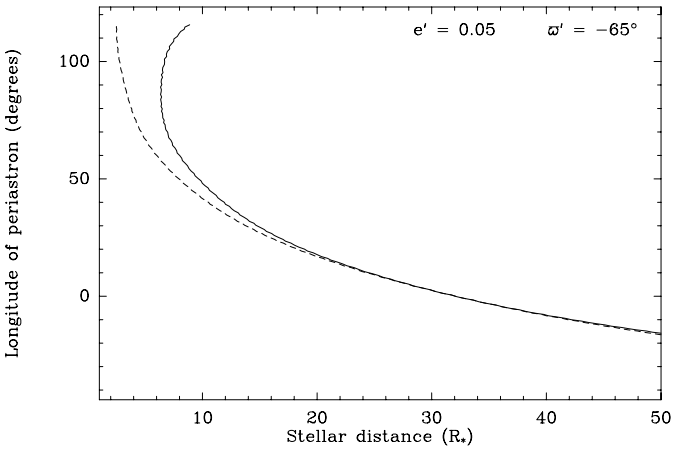

Fig. 11. Variation of the longitude of the periastron as a function of the stellar distance, for FEBs trapped in the 4:1 mean motion resonance with a planet orbiting the star at 10. A.U., having an eccentricity $e' = 0.05$. The longitude of the periastron of the planet with respect to the line of sight is fixed to $\varpi' = -65°$. The longitude of the periastron of the FEBs gradually change when their periastron decreases. On the solid line, ϖ is plotted as a function of the actual stellar distance of the bodies when crossing the line of sight. On the dashed line, it is plotted as a function of their periastron distance

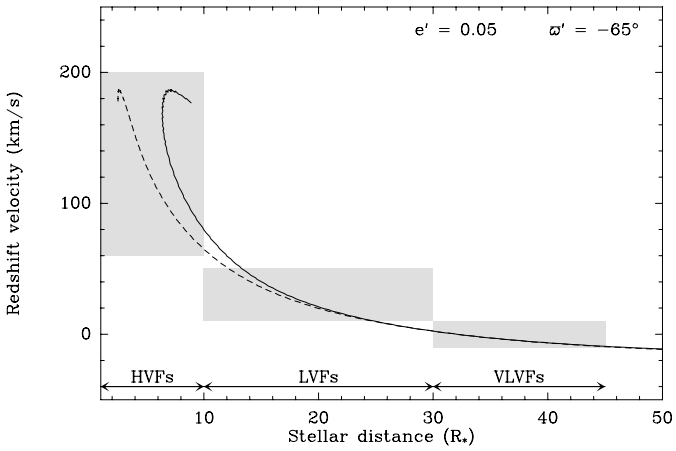

Fig. 12. Same as Fig. 10, but for FEBs having a longitude of periastron varying as a function of the periastron according to Fig. 11. The plotting conventions for the solid and the dashed lines are the same as for Fig. 11: on the solid line the velocity of the variable events is plotted as a function of the actual stellar distance of the bodies when they cross the line of sight; on the dashed line, the same velocity, i.e. corresponding to the time they cross the line of sight, is plotted as a function of the periastron distance. Of course, only the solid line must be considered for comparison purpose with the grey boxes, but comparing the two curves illustrates how far the bodies are from periastron when crossing the line of sight

Fig. 10 illustrates that a constant longitude of periastron cannot account for all FEBs, irrespective to their periastron distance. In this figure, the expected redshift velocity of the FEBs is plotted as a function of stellar distance, for a constant $\varpi = 20°$. This calculation is based on Eq. 14, but individual runs of the complete simulation show that the obtained redshifts perfectly match this theoretical behavior. In other words, the redshift velocity of a given FEB corresponds exactly to the projection of its velocity relative to the star onto the line of sight when crossing it.

The value $\varpi = 20°$ was chosen in order to fit the redshift range for LVFs. Indeed, the observed velocities of LVFs are correctly fitted on Fig. 10. The fit is however not fully satisfactory for HVFs. Even if their velocity is larger (due to a larger net velocity on the orbit), they hardly reach more than 100 km s^{-1}. The fit is even worse for VLVFs, who should never be seen at velocities less than 15 km s^{-1}, apart from statistical departures around the mean ϖ value. It turns out that no fixed value for ϖ can account for all kinds of variables features observed in the Ca II line toward β Pictoris. While fitting properly the LVFs require $\varpi \simeq 20°$, the HVFs are better fitted with $\varpi \simeq 40°$ or even more, and the for the VLVFs we need ϖ values around $0°$.

5.3. Link with the mean-motion resonance model

As it seems that accounting for all the variety of the observed features requires the longitude of the periastron of the FEBs to be a function of the periastron distance, although still varying within a rather limited range, it would now be interesting to see whether this new picture is compatible with the suspected dynamical process generating the FEB phenomenon, namely

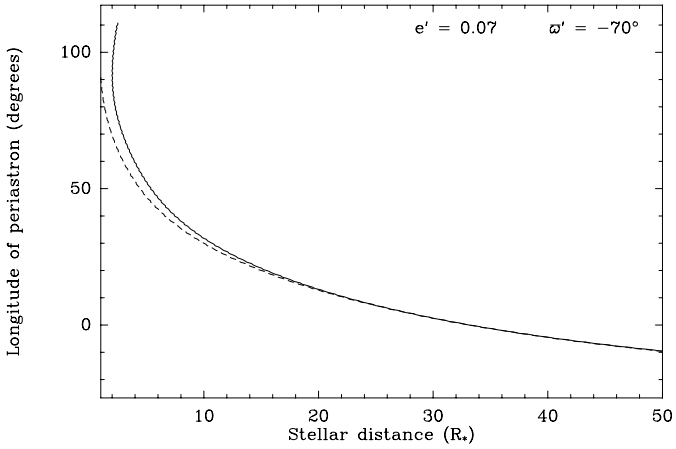

Fig. 13. Same as Fig. 11, but for a planet following an orbit with an eccentricity $e' = 0.07$ and a longitude of periastron $\varpi' = -70°$

the mean-motion resonance model. In fact it is, as explained below, and this may help us to further constrain this model.

In Beust & Morbidelli (1996), several phase-portrait diagrams are shown, illustrating the topology of the resonant dynamics in our case of interest. These figures show in particular that as soon as the eccentricity of the perturbing planet e' is $\gtrsim 0.05$, particles trapped into the 4:1 mean-motion resonance are subject to evolve up to eccentricity $e \simeq 1$, and at the time they reach this value, their longitude of periastron is constrained to $\sim 180°$ with respect to that of the planet. This is the basic picture for explaining a non-axisymmetric FEB infall.

We may see however (in particular in Fig. 11 from Beust & Morbidelli, 1996) that whenever the periastron of the

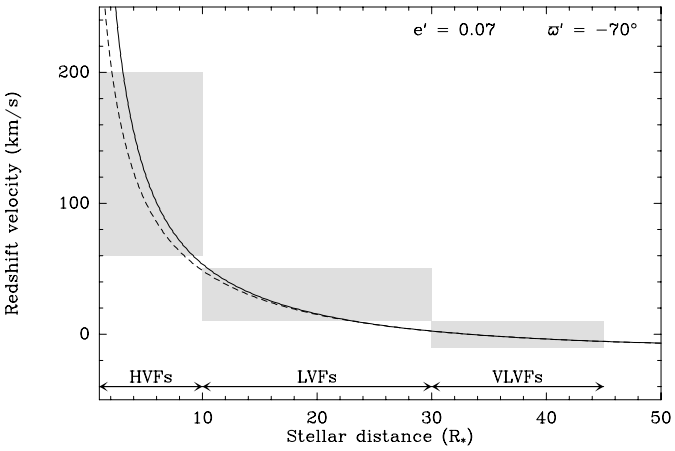

Fig. 14. Same as Fig. 12, but for FEBs having a longitude of periastron varying according to Fig. 13

particle decreases, its longitude of periastron (relatively to that of the planet) gradually evolves, and reaches $180°$ when the minimum periastron value is reached. Consequently, FEBs still having a periastron of $30\,R_*$ should not have the same longitude of periastron that those having a periastron of $5\,R_*$, i.e., exactly what we seem to derive from observational constraints. Moreover, if we believe the orbits to be prograde, we see in Fig. 11 from Beust & Morbidelli (1996) that the variation sense of ϖ when the periastron is decreasing is in agreement with the one we seem to require.

Alternatively, one could think that families of FEBs having various might be due to different mean-motion resonances instead of only the 4:1. However, as shown in Beust & Morbidelli (1996), the 4:1 is by far the most powerful resonance. The 4:1 and the 3:1 are the only ones that are able to bring the eccentricities up to FEB-like values ($\gtrsim 0.9$) (see also the study of a larger set of resonances by Yoshikawa, 1989). The 3:1 is probably much less powerful than the 4:1 because it requires the initial eccentricity of the bodies to be $\gtrsim 0.2$–0.35 (depending on the eccentricity of the planet) in order to make them evolve towards star-grazing orbits, while in the 4:1 resonance, even bodies with initial zero eccentricity are subject to become FEBs. The strength of the 3:1 resonance (with Jupiter) is however enhanced in the Solar System by the overlap of secular resonances *inside* mean-motion resonances (Morbidelli & Moons, 1995). If such a model cannot be excluded for β Pic, it remains highly putative.

The free parameters of the 4:1 mean-motion resonance model are the mass of the planet, its semi-major axis a', its eccentricity e', and also its longitude of periastron ϖ' relative to the line of sight. As already noted in Beust & Morbidelli (1996), the mass of the planet does not affect very much the dynamics of particles trapped into the 4:1 mean motion resonance. We assumed in the following application a mass ratio of 0.001 with respect with the planet, i.e., a Jupiter-like planet. Assuming a smaller planet just shrinks the size of the resonant region in the (a, e) planet (this leading to less potential star-grazers) without very much affecting the dynamics of those particle which are actually trapped. For statistical reasons (i.e., the high number of observed FEBs), a gaseous giant seems better suited than an Earth-sized planet. The semi-major axis a' is just a scaling parameter, as the restricted 3-body problem is scale invariant.

We first assumed $e' = 0.05$ as this is enough for the 4:1 resonance to be an active source of FEBs. We did careful numerical integrations using the Extended Schubart Integrator (Moons, 1994), an averaged integrator dedicated for resonant dynamics and we obtained for various cases the value of the longitude of periastron (relative to the planet) whenever the particle approaches $e = 1$. We afterwards tried several values for ϖ' and a' in order to fix the longitudes of periastra and the periastron distances, trying to fit the observing boxes displayed on Fig. 10.

Our best fit for $e' = 0.05$ is shown on Figs. 11 and 12, achieved for $a' = 10$ A.U. and $\varpi' = -65°$. Fig. 11 plots the longitude of periastron of the FEBs as a function of the periastron distance, and also as a function of the stellar distance when crossing the line of sight. Both do not coincide, because the FEBs are not exactly at periastron when they cross the line of sight. Fig. 12 is equivalent to Fig. 10, but we take now into account the variation of ϖ plotted in Fig. 10. We see that the fit is now much better than on Fig. 10, showing that the variation of ϖ as a function of the periastron is actually well suited for our purpose.

However, we feel it not totally satisfactory, essentially because the FEBs cannot get closer to the star than $\sim 6\,R_*$. Closer approaches (down to $1-2\,R_*$) are necessary, because these are the only ones that are able to explain the very-high velocity events ($> 200\,\mathrm{km\,s^{-1}}$) sometimes observed in the UV lines of Al III or Mg II (Lagrange-Henri et al., 1988, 1989). We do not have close approaches because whenever $q \gtrsim 10\,R_*$, ϖ becomes high enough (Fig. 11) to make the FEBs to pass across the line of sight at a stellar distance d significantly larger than q. In order to solve this problem, we may decrease the longitude of the periastron of the planet ϖ' down to -80 or $-90°$, but in that case, the corresponding velocities we obtain for the VLVFs, and even for the LVFs, move significantly to strongly blueshifted values, that no not match the observing boxes. Note that assuming ϖ' values out of the range -100 to $10°$ leads either to no observable FEB, or to unrealistic velocities. In fact the convenient range for ϖ' to account for both the LVFs and the VLVFs is $-65 \pm 5°$.

On could also decrease the value of the semi-major axis of the planet a'. As the problem simply rescales with a', reducing a' causes the minimum approach to decrease. It appears however necessary to reduce a' down to less than 3 A.U. in order to allow vary close approaches to be (even still hardly) compatible to all the constraints. Such a small value seems unrealistic to us. At such a small stellar distance, the orbital period would be 3.9 yr, and that of the FEBs would by roughly 1 year, while their semi-major axis would be 1.2 A.U.. According to the resonant dynamics (see Beust & Morbidelli, 1996), we would expect the overall frequency of FEB arrival to present a sinusoidal modulation with a period of 1 year, which was not observed. In fact, even if no evident periodicity was yet observed, it appears ob-

vious that this overall frequency exhibits drastic changes over a time-scale of the order of 2 years. If this is the signature of a periodic behavior, its period should be of the order of at least 5 yr. This is why $a' = 10$ A.U. may be considered a a plausible value for the planetary semi-major axis, although this last parameter is very hard to constrain.

The problem is much better solved assuming a slightly larger value for the planetary eccentricity e', namely 0.07. This is illustrated in Figs. 13 and 14, which are equivalent to Figs. 11 and 12, but for $e' = 0.07$ and $\varpi' = -70°$, the latter value being better suited than $-65°$ in the $e' = 0.07$ case. We now see on Fig. 14 that the theoretical curve bluntly crosses all the observing boxes, and that very high velocity events associated to very close stellar approaches are also allowed. Indeed, in the three simulations displayed on Figs. 7–9, the longitude of the periastron of the FEB was fixed as a function of q accordingly to the $e' = 0.07$, $\varpi' = -70°$ and $a' = 10$ A.U. case. This leads to $\varpi \simeq 20°$ for the LVF generating FEB. This shows how the same model may reproduce all kinds of variable features observed up to now.

5.4. A large scale simulation

All particles trapped in the 4:1 resonance are not subject to follow exactly the solid curve on Fig. 14, because the initial conditions may be slightly different. Hence it is important to check whether the conclusions deduced from a single integration are robust towards variation of initial conditions. Indeed, the following may vary:

- the initial eccentricity and semi-major axis may vary. The computation on Fig. 14 assumes respective initial values of 0.05 and 3.966 A.U. (the exact 4:1 resonance location);
- the orbit may be somewhat inclined. Note that on Fig. 14, the simulation is planar;
- the libration amplitude, controlled by the initial longitude of periastron. On Fig. 14, this amplitude is assumed to be zero. Note that along the resonant motion, this amplitude is secularly conserved as an adiabatic invariant (see Morbidelli & Moons, 1993);
- the initial longitude of periastron: In Fig. 14, $\varpi - \varpi' = 180°$ was initially assumed.

Hence we wanted to test the model over a much large scale, testing bodies with various initial conditions trapped into the resonance. We thus carried out a numerical simulation involving 10,000 bodies, using the Mixed Variable Symplectic integrator developed by Levison et al., once adapted to the β Pic case (Levison & Duncan, 1994; Michel & Valsecchi, 1996), assuming the same planetary data as in Fig. 14 ($a' = 10$ A.U., $e' = 0.07$, $\varpi' = -70°$). The initial semi-major axes were sorted randomly between 3.955 and 3.979 A.U, and the eccentricities between 0 and 0.3, so that most of them are trapped into the 4:1 resonance. The inclinations were sorted randomly between $0°$ and $2°$. All the other orbital angular parameters are sorted randomly, so that all possible initial resonant configurations are described.

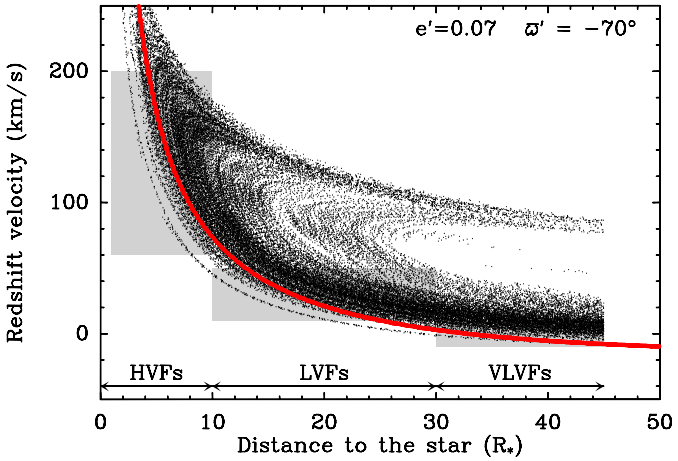

Fig. 15. Result of the integration of 10,000 bodies in the 4:1 resonance, shown in the same manner as in Fig. 14. Each dot corresponds to a computed passage across the line of sight of one body, occurring in the dust evaporation zone ($d \geq 45\,R_*$). As a given body has successive periastron passages, several dots may correspond to the same body, but at various epochs. The thick grey curve corresponds to the solid curve of Fig. 14, displayed for comparison purpose

The result is shown in Fig. 15, which is sketched in the same way as Fig. 14. Each individual dot represents a computed periastron passage across the line of sight, inside the dust evaporation zone. The following conclusions may be drawn:

- The dots follow the "theoretical" curve from Fig. 14, and remain closely confined around it. Moreover, the width in velocity of the main dots area, for a given stellar distance, roughly matches the observational constraints.
- The lower edge of the dots area, i.e. towards blueshifts, is very sharp. Hence blueshifted LVF or HVF-like features are not to be expected from this dynamics;
- There are some events (although less numerous) appearing between around $+100\,\mathrm{km}^{-1}$ in the LVF and event VLVF range that do not match the observations.

These events might exist, but we feel that they are probably much less numerous than might be deduced from Fig. 15. A significant part of these events correspond to bodies having the largest initial eccentricities $\gtrsim 0.2$. They are probably much less numerous that the lower eccentricity ones. Indeed, assuming an initial eccentricity distribution between 0 and 0.2 drastically reduces their number. Moreover, all these events corresponds to bodies that have already gone through their minimal periastron via the resonant dynamics. Hence these bodies undergo a large number of periastron passages well inside the dust evaporation zone before generating events in this area. We believe that most of them are likely to be fully evaporated before. The same applies also of course for HVF generating bodies, but as it may be seen from Fig. 15, HVF events are more numerous that 80–100 $\mathrm{km\,s}^{-1}$ LVF events, so they are more likely to be observed. The real curve, taking into account the gradual destruction of bodies due to evaporation (this will be presented in a forthcoming paper), is probably less dense towards HVF

events, and much less towards 100 km s^{-1} LVF events. This is compatible with the observational statistics.

In conclusion, the 4:1 mean-motion resonance model for FEBs appears robust towards the variation of the initial orbital conditions inside the resonance, and it is well designed to explain the ϖ confinement of FEBs that seems to be required by the data analysis.

The ranges for the orbital parameters of the perturbing planet that are fully compatible with the various constraints are $0.06 \lesssim e'$, $-60° \lesssim \varpi' \lesssim -80°$, and $5\,\mathrm{AU} \gtrsim a' \gtrsim 20\,\mathrm{AU}$. a' is clearly the least constrained parameter. Note also that these data do not put any upper limit to e', but a maximum eccentricity of 0.1 or 0.15 might by considered.

6. Conclusion

Observed with UHRF at a resolution $R = 10^6$, the central circumstellar Ca II absorptions toward β Pictoris appear complex, revealing the presence of time-variable, very low velocity absorption features that could not be separated from the main central component at a lower resolution. The actual central component finally turns out to be much narrower than previously thought. It is however still compatible with the steady-state flow model presented in Lagrange et al. (1998), if we assume the gas for this component to be located around ~ 1.5 A.U. rather than 0.5 A.U..

The very low velocity events still appear compatible with the FEB scenario that was formerly invoked for explaining the higher redshift events. In previous work, we had shown that in the framework of the FEB scenario, the statistics on the velocities on the variable events are much more compatible with a fixed orientation for all the orbits of the FEBs rather than a random distribution. The VLVFs help us refining this picture, showing that the longitude of periastron of the FEBs must be a weakly varying function of their periastron distance. This appears in fact in perfect agreement with the predictions of the mean-motion resonance model proposed by Beust & Morbidelli (1996) as a potential dynamical source for the FEB phenomenon. Hence we may claim that this model is considerably reinforced by the present UHRF observations, as all kinds of variable events appear to be straightforwardly explained by this model with very few free parameters.

This of course does not tell us how long the FEB phenomenon is expected to last within the β Pictoris system. As noted in Beust & Morbidelli (1996), a typical time of $2\,10^5$ planetary revolutions is required to make a resonant body become a FEB. Hence, the characteristic time for clearing the 4:1 resonance should be less than $\sim 10^7$ yr. However, the mechanism could be sustained a somewhat longer time if the resonance is refilled during that time. This may be achieved assuming that the planet may undergo a gradual orbital migration, leading to a displacement of the resonances. This phenomenon probably occurred at the beginning of the history of the Solar System; the outer planets are thought to have migrated exchanging angular momentum with the numerous planetesimals they were ejecting inwards or outwards (Fernandez & Ip, 1984), the migration being significant over a time-scale of the order of 10^8 yr. More recently, Ward (1997) showed that a torque (a tidal interaction) might appear in a forming planetary system between a protoplanet and the circumstellar disk, with the consequence of inward migration for the planet. Hence, observing a still active FEB phenomenon at a typical β Pic age of $\sim 10^8$ yr may not appear surprising. Another related question is whether the FEB phenomenon is a generic mechanism during the formation of planetary systems or not. The similar spectral activity observed in several main sequence (Lecavelier et al., 1997; Cheng et al., 1997) and Herbig stars (Grinin et al., 1994; Grady et al., 1996; Grinin et al., 1996) suggests that it is not limited to the β Pic case. It is quite a tempting hypothesis to suggest that what we observe as a FEB phenomenon toward these stars is only part of the planetesimal clearing out and high bombardment phase that occurred roughly at the same age in the Solar System.

References

Artymowicz P., 1988, ApJ 335, L79

Bertaux J.L., Blamont J.E., Festou M., 1973, A&A 25, 415

Beust H., Lagrange-Henri A.-M., Vidal-Madjar, A., Ferlet, R., 1990, A&A 236, 202

Beust H., Morbidelli A., 1996, Icarus 120, 358

Beust H., Vidal-Madjar A., Ferlet R., Lagrange-Henri, A.M., 1991a, A&A 241, 488

Beust H., Vidal-Madjar A., Ferlet R., 1991b, A&A 247, 505

Beust H., Lagrange A.-M., Plazy F. Mouillet D., 1996, A&A 310, 181

Bohren C.F., Huffmann D.R., 1983, *Absorption and scattering of light by small particles*, J. Wiley and Sons

Bruhweiler F.C., Kondo Y., Grady C.A., 1991, ApJ 377, L49

Cheng K.-P., Bruhweiler F.C., Neff J.E., 1997, ApJ 481, 866

Crawford I.A., Spyromilio J., Barlow M.J., Diego F., Lagrange A.-M., 1994, MNRAS, 266, L65

Crawford I.A., Beust H., Lagrange A.-M., 1998, MNRAS 294, L31

Crifo F., Vidal-Madjar A., Lallement R., Ferlet R.,Gerbaldi M., 1997, A&A 320, L29

Dean J.A., in *Lange's handbook of chemistry*, 1985, McGraw-Hill

Diego F., Fish A.C., Barlow M.J., et al., 1995, MNRAS 272, 323

Draine B.T., Lee H.M., 1984, ApJ 285, 89

Fernandez J.A., Ip W.-H., 1984, Icarus 58, 109

Festou M., Rickman H., West R.M, 1993, A&AR 5, 37

Freudling W., Lagrange A.-M, Vidal-Madjar A., Ferlet R., Forveille T., 1995, A&A 301, 231

Grady C.A, Pérez M.R., Talavera A., et al., 1996, A&AS 120, 157

Grinin V.P. Thé P.S., de Winter D., et al., 1994, A&A 292, 165

Grinin V.P., Kozlova O.V., Thé P.S., Rostopchina A.N., 1996, A&A 309, 474

Henning T., Begemann B., Mutschke H., Dorschner J., 1995, A&AS 112, 143

Hodges R.R., 1990, Icarus 83, 410

Kurucz R.L., 1979, ApJS 40, 1

Lagrange-Henri A.-M., Vidal-Madjar A., Ferlet R. 1988, A&A 190, 275

Lagrange-Henri A.-M., Beust H., Vidal-Madjar A., Ferlet, R.: 1989, A&A 215, L5

Lagrange A.-M., Vidal-Madjar A., Deleuil M., et al., 1995, A&A 296, 499

Lagrange A.-M., Plazy F., Beust H., et al., 1996, A&A 310, 547
Lagrange A.-M., Beust H., Mouillet D., et al., 1998, A&A 330, 1091
Lämmerzahl P., Krankowsky D., Hodges R.R., et al., 1987, A&A 187, 169
Lamy P.L., 1974, A&A 35, 197
Laor A., Draine B.T., 1993, ApJ 402, 441
Lecavelier des Etangs A., Deleuil M., Vidal-Madjar A., 1997, A&A 325, 228
Leger A., Gauthier S., Defourneau D., Rouan D., 1983, A&A 117, 164
Levison H.F., Duncan M.J., 1994, Icarus 108, 18
Levison H.F., Duncan M.J., Wetherill G.W., 1995, Nat 372, 441
Lien D.J., 1990, ApJ 355, 680
Michel P., Valsecchi G.B., 1996, Celest. Mech. 65, 355
Orosei R., Capaccioni F., Capria M.T., et al., 1995, A&A 301, 613
Maxwell-Garnett J.C., 1904, Phil. Trans. R. Soc. A203, 385
Moons M., 1994, Celest. Mech. 60, 173
Mouillet D., Lagrange A.-M., A&A 297, 175
Morbidelli A., Moons M., 1993, Icarus 102, 316
Morbidelli A., Moons M., 1995, Icarus 115, 60
Mukai T., Schwehm G., 1981, A&A 95, 373
Smith B., Terrile R., 1984, Sci 226, 1421
Vidal-Madjar A., Hobbs L.M., Ferlet R., Gry C., Albert C.E., 1986, A&A 167, 325
Vidal-Madjar A., Lagrange-Henri A.-M., Feldman P.D., et al., 1994, A&A 290, 245
Ward W.R., 1997, ApJ 482, L211
Warren S.G., 1984, Appl. Opt. 23, 1206
Warren S.G., 1986, Appl. Opt. 25, 2650
Yoshikawa M., 1989, A&A 213, 436
Zubko V.G., Mennella V., Colangeli L., Bussoletti E., 1996, MNRAS 282, 1321